CSIAM Trans. Life Sci.
doi: 10.4208/csiam-ls.SO-2024-0003

Vol. **1**, No. 1, pp. 45-66
March 2025

The Asymptotic Behavior of Conditional Granger Causality with Respect to Sampling Interval

Jinlong Mei[1,2,3], Kai Chen[1,2,3], Yanyang Xiao[4,5,6],
Songting Li[1,2,3,*] and Douglas Zhou[1,2,3,*]

[1] *School of Mathematical Sciences, Shanghai Jiao Tong University,*
Shanghai 200240, China.
[2] *Institute of Natural Sciences, Shanghai Jiao Tong University,*
Shanghai 200240, China.
[3] *Ministry of Education Key Laboratory of Scientific and Engineering*
Computing, Shanghai Jiao Tong University, Shanghai 200240, China.
[4] *Interdisciplinary Center for Brain Information, the Brain Cognition*
and Brain Disease Institute, Shenzhen Institute of Advanced Technology,
Chinese Academy of Sciences, Shenzhen 518055, China.
[5] *CAS Key Laboratory of Brain Connectome and Manipulation,*
the Brain Cognition and Brain Disease Institute, Shenzhen Institute
of Advanced Technology, Chinese Academy of Sciences, Shenzhen 518055, China.
[6] *Shenzhen-Hong Kong Institute of Brain Science, Shenzhen Institute*
of Advanced Technology, Chinese Academy of Sciences, Shenzhen 518055, China.

Received 21 December 2023; Accepted 22 April 2024

Abstract. Granger causality (GC) stands as a powerful causal inference tool in time series analysis. Typically estimated from time series data with finite sampling rate, the GC value inherently depends on the sampling interval τ. Intuitively, a higher data sampling rate leads to a time series that better approximates the real signal. However, previous studies have shown that the bivariate GC converges to zero linearly as τ approaches zero, which will lead to mis-inference of causality due to vanishing GC value even in the presence of causality. In this work, by performing mathematical analysis, we show this asymptotic behavior remains valid in the case of conditional GC when applying to a system composed of more than two variables. We validate the analytical result by computing GC value with multiple sampling rates for the simulated data of Hodgkin-Huxley neuronal networks and the experimental data of intracranial EEG signals. Our result demonstrates the hazard of GC inference with high sampling rate, and we propose an accurate inference approach by calculating the ratio of GC to τ as τ approaches zero.

AMS subject classifications: 62H20, 62F12, 62J05, 62M10

---

[*] Corresponding author. *Email addresses:* `songting@sjtu.edu.cn` (S. Li), `zdz@sjtu.edu.cn` (D. Zhou)

Key words: Causal inference, conditional Granger causality, sampling rate, asymptotic behavior, Hodgkin-Huxley model.

1 Introduction

The investigation into the structure and function of the brain has always been an important topic in neuroscience research. Within the pursuit of this field, a crucial aspect is to unravel the functional interactions across different neurons or cortical areas in the brain. With the development of neuroscience techniques, from invasive recordings to noninvasive methods [30, 35], activities can be recorded simultaneously from multiple neurons and across different brain areas. And recent years have seen numerous works about functional connectivity and causal modeling [14, 24] based on brain signals, attempting to provide insights into the patterns of brain functionalities. "Functional connectivity" measures the degree of co-activation of neurons or brain areas, which is often calculated by the correlation coefficient between neural time series data. However, correlation coefficient cannot provide directional information about the interactions.

Granger causality (GC), proposed in 1950s, has been introduced to the field of neuroscience since the beginning of this century [5, 6, 11, 12, 37]. GC can infer the direction of causal interactions between neural signals, and has been applied to various types of neural data, including single-cell and multi-cell recordings [4], local field potentials (LFPs) [9,28], electroencephalography (EEG) [17,18], magnetoencephalography (MEG) [13], and functional magnetic resonance imaging (fMRI) [7, 31, 41]. In recent years, there has been a gradual emergence of research focusing on the theoretical basis of applying GC analysis, rooted in the theory of linear regression, to nonlinear neural systems. It has been theoretically established in previous works that GC, despite being a linear method, possesses the capability to extract nonlinear causal interactions within neural systems under certain conditions, and can be applied to reconstructions of the structural connectivity of neuronal networks [2, 8, 12, 33, 43].

However, it has been found that the GC value depends on the sampling interval of the time series, and it may even infer a false causal relationship when the sampling interval is not properly chosen [26]. Further mathematical analysis has been developed to reveal the dependence of GC on sampling interval for a pair of neurons, which showed that the bivariate GC converges to zero linearly as the sampling interval approaches zero. In addition, a practical approach was proposed to reliably estimate the causal relations between nodes in the network [44, 45]. It successfully overcomes the issue of vanishing GC caused by small sampling interval, i.e. high sampling rate in recent experimental measurements, when the original system satisfies certain conditions.

It is noted that the previous analysis mainly focused on the conventional GC on a bivariate system, which limits its applicability to large neural systems composed of more than two variables. In this work, we extend the mathematical analysis to the case of multivariate conditional GC, and show that the asymptotic structure of conditional GC with respect to sampling interval remains to exist, i.e. the conditional GC approaches zero linearly as the sampling interval approaches zero. We numerically verify the analytical result using time series data simulated by a Hodgkin-Huxley (HH) network model and a public data set of the intracranial EEG signals recorded from epilepsy patients.

The paper is organized as follows. In Section 2, we briefly introduce the Hodgkin-Huxley neural network model and the conditional GC analysis. In Section 3, we derive the asymptotic behavior of conditional GC value regarding sampling interval, and verify the asymptotic structure of conditional GC value by analyzing the HH neural network model and the iEEG data recorded from the experiment. In Section 4, we conclude by discussing the feasibility and accuracy of applying conditional GC analysis to real experimental and clinical time series data by exploiting the asymptotic structure of conditional GC.

2 Materials and methods

2.1 The Hodgkin-Huxley model

The Hodgkin-Huxley (HH) model was proposed by Hodgkin and Huxley in early 1950s [19–22], which captures the activity of the membrane potential of a single neuron and the mechanism of action potential generation. The membrane potential dynamics of the *i*-th HH neuron in a network is governed by the following equations:

$$\begin{aligned}
&C\frac{\mathrm{d}V_i}{\mathrm{d}t}=-(V_i-V_{\mathrm{Na}})G_{\mathrm{Na}}m_i^3h_i-(V_i-V_{\mathrm{K}})G_{\mathrm{K}}n_i^4-(V_i-V_{\mathrm{L}})G_{\mathrm{L}}+I_i^{\mathrm{input}},\\
&\frac{\mathrm{d}m_i}{\mathrm{d}t}=(1-m_i)\alpha_m(V_i)-m_i\beta_m(V_i),\\
&\frac{\mathrm{d}h_i}{\mathrm{d}t}=(1-h_i)\alpha_h(V_i)-h_i\beta_h(V_i),\\
&\frac{\mathrm{d}n_i}{\mathrm{d}t}=(1-n_i)\alpha_n(V_i)-n_i\beta_n(V_i),
\end{aligned}$$

where

$$\begin{aligned}
&\alpha_n(V_i)=\frac{0.1-V_i/100}{\exp(1-V_i/10)-1}, &&\beta_n(V_i)=0.125\exp\left(-\frac{V_i}{80}\right),\\
&\alpha_m(V_i)=\frac{2.5-V_i/10}{\exp(2.5-V_i/10)-1}, &&\beta_m(V_i)=4\exp\left(-\frac{V_i}{18}\right),\\
&\alpha_h(V_i)=0.07\exp\left(-\frac{V_i}{20}\right), &&\beta_h(V_i)=\frac{1}{\exp(3-V_i/10)+1}.
\end{aligned}$$

Here, C is the membrane capacitance and V_i is the membrane potential, m_i,h_i,n_i are gating variables of sodium and potassium ionic channels. And $V_{\mathrm{Na}},V_{\mathrm{K}},V_{\mathrm{L}}$ are the reversal potential of sodium, potassium and leaky currents, respectively, $G_{\mathrm{Na}},G_{\mathrm{K}},G_{\mathrm{L}}$ are the conductance of sodium, potassium and leaky currents, respectively. I_i^{input} is the total input current to the i-th neuron. The parameters above are set as $C=1\,\mu\mathrm{F}\cdot\mathrm{cm}^{-2}, V_{\mathrm{Na}}=115\,\mathrm{mV}$, $V_{\mathrm{K}}=-12\mathrm{mV}, V_{\mathrm{L}}=10.6\mathrm{mV}, G_{\mathrm{Na}}=120\mathrm{mS}\cdot\mathrm{cm}^{-2}, G_{\mathrm{K}}=36\mathrm{mS}\cdot\mathrm{cm}^{-2}, G_{\mathrm{L}}=0.3\mathrm{mS}\cdot\mathrm{cm}^{-2}$. Here all voltages are relative to the resting potential [15].

The kinetics of the input current to i-th neuron is modeled by

$$\begin{aligned} I_i^{\text{input}} &= I_i^{\mathrm{E}}+I_i^{\mathrm{I}},\\ I_i^{\mathrm{E}} &= -\left(V_i-V_G^{\mathrm{E}}\right)G_i^{\mathrm{E}},\\ I_i^{\mathrm{I}} &= -\left(V_i-V_G^{\mathrm{I}}\right)G_i^{\mathrm{I}}, \end{aligned}$$

where I_i^{E} (I_i^{I}) represents the excitatory (inhibitory) input that the i-th neuron received. V_G^{E} (V_G^{I}) is the corresponding reversal potential, with $V_G^{\mathrm{E}}=65\,\mathrm{mV}$ ($V_G^{\mathrm{I}}=-15\,\mathrm{mV}$). The dynamics of conductance G_i^{E} (G_i^{I}) is governed by [29]

$$\begin{aligned} \frac{\mathrm{d}G_i^{\mathrm{E}}}{\mathrm{d}t} &= -\frac{G_i^{\mathrm{E}}}{\sigma_d^{\mathrm{E}}}+H_i^{\mathrm{E}},\\ \frac{\mathrm{d}G_i^{\mathrm{I}}}{\mathrm{d}t} &= -\frac{G_i^{\mathrm{I}}}{\sigma_d^{\mathrm{I}}}+H_i^{\mathrm{I}},\\ \frac{\mathrm{d}H_i^{\mathrm{E}}}{\mathrm{d}t} &= -\frac{H_i^{\mathrm{E}}}{\sigma_r^{\mathrm{E}}}+\sum_k F_i^{\mathrm{E}}\delta\left(t-T_{i,k}^{\mathrm{E}}\right)+\sum_{j\neq i}\left(S^{\mathrm{EE}}\delta_{\mathrm{E},Q_i}\delta_{\mathrm{E},Q_j}+S^{\mathrm{IE}}\delta_{\mathrm{I},Q_i}\delta_{\mathrm{E},Q_j}\right)m_{ij}g\left(V_j^{\mathrm{pre}}\right),\\ \frac{\mathrm{d}H_i^{\mathrm{I}}}{\mathrm{d}t} &= -\frac{H_i^{\mathrm{I}}}{\sigma_r^{\mathrm{I}}}+\sum_{j\neq i}\left(S^{\mathrm{EI}}\delta_{\mathrm{E},Q_i}\delta_{\mathrm{I},Q_j}+S^{\mathrm{II}}\delta_{\mathrm{I},Q_i}\delta_{\mathrm{I},Q_j}\right)m_{ij}g\left(V_j^{\mathrm{pre}}\right), \end{aligned}$$

where the synaptic input from the pre-synaptic neuron to the post-synaptic variable $H_i^E(H_i^I)$ shapes as a sigmoid function [10,32]

$$g\left(V_j^{\mathrm{pre}}\right)=\frac{1}{1+\exp\left(-\left(V_j^{\mathrm{pre}}-85\right)/2\right)}.$$

Here, σ_r^{E} (σ_r^{I}) and σ_d^{E} (σ_d^{I}) are the rising and decaying time constants of the input conductance G_i^{E} (G_i^{I}), with the value σ_r^{E}=0.5ms, σ_r^{I}=0.5ms, σ_d^{E}=3.0ms, σ_d^{I}=7.0ms. The i-th neuron is driven by independent excitatory homogeneous Poisson input (Poisson process) with input strength F_i^{E} and rate μ_i^{E}. In this work, all neurons receive Poisson inputs with the same strength $F_i^{\mathrm{E}}=F^{\mathrm{E}}$ and rate $\mu_i^{\mathrm{E}}=\mu^{\mathrm{E}}$. $T_{i,k}^{\mathrm{E}}$ indicates the arriving time of k-th input pulse received by the i-th neuron, which differs from neuron to neuron.

The connection among HH neurons in the network is depicted by a binary adjacency matrix $\boldsymbol{M}=(m_{ij})$, with $m_{ij}=1$ indicating a direct connection from neuron j to neuron i and $m_{ij}=0$ indicating no direct connection. The coupling strength from a neuron of type Q_j to a neuron of type Q_i is $S^{Q_iQ_j}$ ($Q_i,Q_j\in\{\mathrm{E},\mathrm{I}\}$, where E is for excitatory, and I is for inhibitory). δ_{Q_i,Q_j} represents the Kronecker delta function taking the value of 1 when $Q_i=Q_j$ and otherwise 0. And V_j^{pre} is the membrane potential of the j-th neuron as a presynaptic neuron.

In this model, when the membrane potential $V_j(t)$ exceeds the threshold at around $15\,\mathrm{mV}$, it will rapidly ramp up to near $100\,\mathrm{mV}$ in a few milliseconds and then quickly decay back to form a sharp spike, which is known as the action potential. Whenever an excitatory (inhibitory) neuron fires a spike, it will induce a sharp increment on the variables H_i^E (H_i^I) of its post-synaptic neurons, defined by the adjacency matrix $\boldsymbol{M}$. As a consequence, the conductance of excitatory (inhibitory) input current increases followed by the corresponding change in the membrane potential of the post-synaptic neuron. Therefore, the causal relation between the membrane potentials of a pre-post neuron pair is conducted through its synaptic coupling term. Our previous studies have shown that this causal relation can be captured by GC analysis [42, 43].

2.2 Conditional Granger causality

Granger causality analysis operates under the premise that if incorporating the history of time series y_t reduces the prediction error for another time series x_t, then a causal influence from y_t to x_t exists [25, 34, 38, 39]. While conventional GC analysis is initially formulated in a bivariate context, it can be naturally extended to a multivariate form as the conditional GC [16]. Here we briefly revisit the conditional GC in a trivariate setting for the sake of later elaborations.

Let $X_t=(x_t,\,y_t,\,z_t)^\top$, where x_t, y_t and z_t are three stationary zero-mean discrete time series satisfying the following conditions:

1. $\mathbb{E}(X_t)=\mathbf{0}$ for any $t\in\mathbb{Z}$,
2. $\mathrm{cov}(X_{t_1},\,X_{t_1-j})=\mathrm{cov}(X_{t_2},\,X_{t_2-j})$ for any $t_1,t_2,j\in\mathbb{Z}$,
3. $|\Sigma|>0$.

Here $\Sigma=\mathrm{var}(X_t)$ represents the covariance matrix of X_t and $|\cdot|$ means the determinant of a matrix.

To assess the improvement of prediction of x_t purely by the history of y_t, we need to exclude the influence of the history of z_t. To achieve that, we first apply an "auto-regression" model to fit x_t given the history information of x_t and z_t

$$x_t=\sum_{j=1}^{\infty}b_j^{(x)}x_{t-j}+\sum_{j=1}^{\infty}b_j^{(z)}z_{t-j}+\epsilon_t, \tag{2.1}$$

where $b_j^{(x)}$ and $b_j^{(z)}$ are the regression coefficients of the j-th order history of x_t and z_t, respectively, and ϵ_t is the fitting residual indicating the prediction error of the model. Next, we apply a "joint-regression" model to fit x_t again given the history information of x_t, y_t and z_t

$$x_t=\sum_{j=1}^{\infty}a_j^{(x)}x_{t-j}+\sum_{j=1}^{\infty}a_j^{(y)}y_{t-j}+\sum_{j=1}^{\infty}a_j^{(z)}z_{t-j}+\eta_t, \tag{2.2}$$

where $a_j^{(x)}, a_j^{(y)}$ and $a_j^{(z)}$ are the regression coefficients of the j-th order history of x_t, y_t and z_t, respectively, where η_t is the fitting residual. The conditional GC from y_t to x_t conditioned on z_t is defined by

$$F_{y\to x|z} = \ln\frac{\text{var}(\epsilon_t)}{\text{var}(\eta_t)}, \tag{2.3}$$

It is worth noting that $\text{var}(\eta_t) \leq \text{var}(\epsilon_t)$, since the prediction cannot worsen after incorporating the history of an additional time series y_t. Therefore, $F_{y\to x|z} \geq 0$. In addition, we can also describe conditional GC in the frequency domain [36], details will be explained in the next section.

3 Results

3.1 The derivation of asymptotic behavior of conditional GC

To infer the causal interactions in a system with continuous dynamics, practically we first measure the activity signals with a certain sampling rate, and then perform the GC analysis for the measured discrete time series. Therefore, the conditional GC calculated from the discrete time series is a function of sampling interval τ, we thus denote it by $F_{y\to x|z}^{(\tau)}$. In this section, we will show that $F_{y\to x|z}^{(\tau)}$ tends to zero linearly as τ approaches zero.

We denote the power spectrum matrix of X_t with sampling interval τ as $S^{(\tau)}(\omega)$, where $S^{(\tau)}(\omega) = \mathbb{E}(\tilde{X}(\omega)\tilde{X}(\omega)^*)$, and $\tilde{\cdot}$ means discrete-time Fourier transform and $\cdot^*$ means conjugate transpose. It has been proved that there exists a unique decomposition under the condition that: (i) $S^{(\tau)}(\omega)$ is of full rank almost everywhere and (ii) the integral $\int_{-\pi}^{\pi}\ln|S^{(\tau)}(\omega)|d\omega$ is convergent

$$S^{(\tau)}(\omega) = A^{(\tau)}(e^{\mathrm{i}\omega})A^{(\tau)}(e^{\mathrm{i}\omega})^*,$$

where $A^{(\tau)}(z)$ and $A^{(\tau)}(z)^{-1}$ are analytic inside the unit disk and $A^{(\tau)}(0)$ is real, upper triangular with positive diagonal coefficients [40]. Set $H^{(\tau)}(\omega) = A^{(\tau)}(e^{\mathrm{i}\omega})A^{(\tau)}(0)^{-1}$ and $\Sigma^{(\tau)} = A^{(\tau)}(0)A^{(\tau)}(0)^*$, then $S^{(\tau)}(\omega)$ can be decomposed as

$$S^{(\tau)}(\omega) = H^{(\tau)}(\omega)\Sigma^{(\tau)}H^{(\tau)}(\omega)^*. \tag{3.1}$$

According to the mean value property of an analytic function, we have

$$\frac{1}{2\pi}\int_{-\pi}^{\pi} H^{(\tau)}(\omega)\mathrm{d}\omega = I.$$

Denote f as the frequency of the continuous-time process, and $\omega \in [-\pi,\pi]$ as the frequency of corresponding discrete time series sampled from the continuous-time process.

They have the relation as $\omega=2\pi\tau f$. Then we obtain

$$\int_{-\frac{1}{2\tau}}^{\frac{1}{2\tau}}\tau H^{(\tau)}(2\pi\tau f)\mathrm{d}f=I,$$

which implies that the entities of $H^{(\tau)}$ are scaled by $1/\tau$ as $\tau\to 0$. Combining to the scaling of $S^{(\tau)}$ and $H^{(\tau)}$, we know that $\Sigma^{(\tau)}$ is scaled as τ as $\tau\to 0$. Here we define $\hat{H}(f)=\lim_{\tau\to 0}\tau H^{(\tau)}(\omega)$ and $\hat{\Sigma}=\lim_{\tau\to 0}\Sigma^{(\tau)}/\tau$ [44]. As τ approaching $0, S^{(\tau)}(\omega)/\tau$ converges to the power spectrum matrix for the original continuous-time series.

For ease of illustration, we use the ternary variable as an example, i.e. $X_t=(x_t, y_t, z_t)^\top$ [12]. And we denote $S_1^{(\tau)}(\omega)=S^{(\tau)}(\omega)$, i.e.

$$S_1^{(\tau)}(\omega)=\begin{bmatrix} S_{xx}^{(\tau)}(\omega) & S_{xy}^{(\tau)}(\omega) & S_{xz}^{(\tau)}(\omega)\\ S_{yx}^{(\tau)}(\omega) & S_{yy}^{(\tau)}(\omega) & S_{yz}^{(\tau)}(\omega)\\ S_{zx}^{(\tau)}(\omega) & S_{zy}^{(\tau)}(\omega) & S_{zz}^{(\tau)}(\omega)\end{bmatrix},$$

according to Eq. (3.1), we have

$$S_1^{(\tau)}(\omega)=H^{(\tau)}(\omega)\Sigma^{(\tau)}H^{(\tau)}(\omega)^*,$$

and

$$\lim_{\tau\to 0}\tau H^{(\tau)}(\omega)=\hat{H}(f),\quad \lim_{\tau\to 0}\frac{1}{\tau}\Sigma^{(\tau)}=\hat{\Sigma}.$$

We denote the sub-matrix of $S_1^{(\tau)}$ as

$$S_2^{(\tau)}(\omega)=\begin{bmatrix} S_{xx}^{(\tau)}(\omega) & S_{xz}^{(\tau)}(\omega)\\ S_{zx}^{(\tau)}(\omega) & S_{zz}^{(\tau)}(\omega)\end{bmatrix},$$

and we have a similar decomposition

$$S_2^{(\tau)}(\omega)=G^{(\tau)}(\omega)\Omega^{(\tau)}G^{(\tau)}(\omega)^*,$$

and

$$\lim_{\tau\to 0}\tau G^{(\tau)}(\omega)=\hat{G}(f),\quad \lim_{\tau\to 0}\frac{1}{\tau}\Omega^{(\tau)}=\hat{\Omega}.$$

Previous works [12] have derived the conditional GC in the frequency domain as

$$F_{y\to x|z}^{(\tau)}=\frac{1}{2\pi}\int_{-\pi}^{\pi}\ln\frac{\Omega_{xx}^{(\tau)}}{Q_{xx}^{(\tau)}(\omega)\Sigma_{xx}^{(\tau)}Q_{xx}^{(\tau)}(\omega)^*}\mathrm{d}\omega, \tag{3.2}$$

where

$$Q^{(\tau)}(\omega)=\begin{bmatrix} Q_{xx}^{(\tau)}(\omega) & Q_{xy}^{(\tau)}(\omega) & Q_{xz}^{(\tau)}(\omega) \\ Q_{yx}^{(\tau)}(\omega) & Q_{yy}^{(\tau)}(\omega) & Q_{yz}^{(\tau)}(\omega) \\ Q_{zx}^{(\tau)}(\omega) & Q_{zy}^{(\tau)}(\omega) & Q_{zz}^{(\tau)}(\omega) \end{bmatrix}=\begin{bmatrix} \bar{G}_{xx}^{(\tau)}(\omega) & 0 & \bar{G}_{xz}^{(\tau)}(\omega) \\ 0 & 1 & 0 \\ \bar{G}_{zx}^{(\tau)}(\omega) & 0 & \bar{G}_{zz}^{(\tau)}(\omega) \end{bmatrix}^{-1} \bar{H}^{(\tau)}(\omega),$$

and

$$\begin{aligned} \bar{H}^{(\tau)}(\omega)&=\begin{bmatrix} \bar{H}_{xx}^{(\tau)}(\omega) & \bar{H}_{xy}^{(\tau)}(\omega) & \bar{H}_{xz}^{(\tau)}(\omega) \\ \bar{H}_{yx}^{(\tau)}(\omega) & \bar{H}_{yy}^{(\tau)}(\omega) & \bar{H}_{yz}^{(\tau)}(\omega) \\ \bar{H}_{zx}^{(\tau)}(\omega) & \bar{H}_{zy}^{(\tau)}(\omega) & \bar{H}_{zz}^{(\tau)}(\omega) \end{bmatrix}=H^{(\tau)}(\omega){P_1^{(\tau)}}^{-1}, \\ \bar{G}^{(\tau)}(\omega)&=\begin{bmatrix} \bar{G}_{xx}^{(\tau)}(\omega) & \bar{G}_{xz}^{(\tau)}(\omega) \\ \bar{G}_{zx}^{(\tau)}(\omega) & \bar{G}_{zz}^{(\tau)}(\omega) \end{bmatrix}=G^{(\tau)}(\omega){P_2^{(\tau)}}^{-1}, \\ P_1^{(\tau)}&=\begin{bmatrix} 1 & 0 & 0 \\ 0 & 1 & 0 \\ 0 & -\dfrac{\Sigma_{zy}^{(\tau)}-\Sigma_{zx}^{(\tau)}\Sigma_{xy}^{(\tau)}/\Sigma_{xx}^{(\tau)}}{\Sigma_{yy}^{(\tau)}-\Sigma_{yx}^{(\tau)}\Sigma_{xy}^{(\tau)}/\Sigma_{xx}^{(\tau)}} & 1 \end{bmatrix}\begin{bmatrix} 1 & 0 & 0 \\ -\dfrac{\Sigma_{yx}^{(\tau)}}{\Sigma_{xx}^{(\tau)}} & 1 & 0 \\ -\dfrac{\Sigma_{zx}^{(\tau)}}{\Sigma_{xx}^{(\tau)}} & 0 & 1 \end{bmatrix}, \\ P_2^{(\tau)}&=\begin{bmatrix} 1 & 0 \\ -\dfrac{\Omega_{zx}^{(\tau)}}{\Omega_{xx}^{(\tau)}} & 1 \end{bmatrix}. \end{aligned}$$

Since

$$\lim_{\tau\to 0}\frac{1}{\tau}\Sigma^{(\tau)}=\hat{\Sigma}, \quad \lim_{\tau\to 0}\frac{1}{\tau}\Omega^{(\tau)}=\hat{\Omega},$$

the limit of $P_1^{(\tau)}$ and $P_2^{(\tau)}$ exist, which are denoted as $\hat{P}_1=\lim_{\tau\to 0}P_1^{(\tau)},\hat{P}_2=\lim_{\tau\to 0}P_2^{(\tau)}$, respectively. Moreover, since

$$\lim_{\tau\to 0}\tau H^{(\tau)}(\omega)=\hat{H}(f), \quad \lim_{\tau\to 0}\tau G^{(\tau)}(\omega)=\hat{G}(f),$$

the limit of $\tau\bar{H}^{(\tau)}(\omega)$ and $\tau\bar{G}^{(\tau)}(\omega)$ exist and are denoted as

$$\begin{aligned} \hat{\bar{H}}(f)&=\lim_{\tau\to 0}\tau\bar{H}^{(\tau)}(2\pi\tau f)=\lim_{\tau\to 0}\tau H^{(\tau)}(2\pi\tau f){P_1^{(\tau)}}^{-1}=\hat{H}(f)\hat{P}_1^{-1}, \\ \hat{\bar{G}}(f)&=\lim_{\tau\to 0}\tau\bar{G}^{(\tau)}(2\pi\tau f)=\lim_{\tau\to 0}\tau G^{(\tau)}(2\pi\tau f){P_2^{(\tau)}}^{-1}=\hat{G}(f)\hat{P}_2^{-1}. \end{aligned}$$

We can further compute the limit $\hat{Q}_{xx}(f)$ of $Q^{(\tau)}_{xx}(\omega)$ as

$$\begin{aligned}\hat{Q}_{xx}(f)&=\lim_{\tau\to 0}Q^{(\tau)}_{xx}(2\pi\tau f)\\&=\lim_{\tau\to 0}\frac{\bar{H}^{(\tau)}_{xx}(2\pi\tau f)-\bar{G}^{(\tau)}_{xz}(2\pi\tau f)\bar{G}^{(\tau)}_{zz}(2\pi\tau f)^{-1}\bar{H}^{(\tau)}_{zx}(2\pi\tau f)}{\bar{G}^{(\tau)}_{xx}(2\pi\tau f)-\bar{G}^{(\tau)}_{xz}(2\pi\tau f)\bar{G}^{(\tau)}_{zz}(2\pi\tau f)^{-1}\bar{G}^{(\tau)}_{zx}(2\pi\tau f)}\\&=\frac{\hat{\bar{H}}_{xx}(f)-\hat{\bar{G}}_{xz}(f)\hat{\bar{G}}_{zz}(f)^{-1}\hat{\bar{H}}_{zx}(f)}{\hat{\bar{G}}_{xx}(f)-\hat{\bar{G}}_{xz}(f)\hat{\bar{G}}_{zz}(f)^{-1}\hat{\bar{G}}_{zx}(f)}.\end{aligned}$$

By multiplying $1/\tau$ on both sides of Eq. (3.2), and substituting $\omega=2\pi\tau f$ for ω, we have

$$\begin{aligned}\frac{1}{\tau}F^{(\tau)}_{y\to x|z}&=\frac{1}{2\pi\tau}\int_{-\frac{1}{2\tau}}^{\frac{1}{2\tau}}\ln\frac{(1/\tau)\Omega^{(\tau)}_{xx}}{Q^{(\tau)}_{xx}(\omega)(1/\tau)\Sigma^{(\tau)}_{xx}Q^{(\tau)}_{xx}(\omega)^*}\mathrm{d}2\pi\tau f\\&=\int_{-\frac{1}{2\tau}}^{\frac{1}{2\tau}}\ln\frac{(1/\tau)\Omega^{(\tau)}_{xx}}{Q^{(\tau)}_{xx}(\omega)(1/\tau)\Sigma^{(\tau)}_{xx}Q^{(\tau)}_{xx}(\omega)^*}\mathrm{d}f.\end{aligned}$$

Finally, by letting τ approach 0, with $\|\hat{Q}_{xx}(f)\|$ being continuous and bounded, we can obtain

$$\lim_{\tau\to 0}\frac{1}{\tau}F^{(\tau)}_{y\to x|z}=\int_{-\infty}^{\infty}\ln\frac{\hat{\Omega}_{xx}}{\hat{Q}_{xx}(f)\hat{\Sigma}_{xx}\hat{Q}_{xx}(f)^*}\mathrm{d}f. \tag{3.3}$$

From Eq. (3.3) with the condition that the integral is bounded, the conditional GC will tend to zero linearly as τ approaches zero.

It is worth mentioning that, in a previous work, Zhou *et al.* [44] has proved that, for the unconditional GC $F^{(\tau)}_{y\to x}$, we have

$$\lim_{\tau\to 0}\frac{1}{\tau}F^{(\tau)}_{y\to x}=\int_{-\infty}^{\infty}\ln\frac{P_{xx}(f)}{\hat{\bar{H}}_{xx}(f)\hat{\Sigma}_{xx}\hat{\bar{H}}_{xx}(f)^*}\mathrm{d}f,$$

where $P_{xx}(f)$ is the power spectrum density of the continuous dynamics of x_t, which is the asymptotic form of

$$F^{(\tau)}_{y\to x}=\frac{1}{2\pi}\int_{-\pi}^{\pi}\ln\frac{S^{(\tau)}_{xx}(\omega)}{\bar{H}^{(\tau)}_{xx}(\omega)\Sigma^{(\tau)}_{xx}\bar{H}^{(\tau)}_{xx}(\omega)^*}\mathrm{d}\omega.$$

Next, we will demonstrate that the above result is a special case of conditional GC when x_t and z_t are independent. In such a case, the conditional GC $F^{(\tau)}_{y\to x|z}$ becomes unconditional GC $F^{(\tau)}_{y\to x}$.

Assuming x_t and z_t are independent, we have

$$\bar{G}^{(\tau)}_{xz}(\omega)=G^{(\tau)}_{xz}(\omega)=0,$$

which leads to

$$Q_{xx}^{(\tau)}(\omega)=\frac{\bar{H}_{xx}^{(\tau)}(\omega)}{\bar{G}_{xx}^{(\tau)}(\omega)}=\frac{H_{xx}^{(\tau)}(\omega)+\Sigma_{yx}^{(\tau)}/\Sigma_{xx}^{(\tau)}\cdot H_{xy}^{(\tau)}(\omega)}{G_{xx}^{(\tau)}(\omega)}.$$

By substituting the expression of $Q_{xx}^{(\tau)}(\omega)$ into Eq. (3.2), we can obtain

$$\begin{aligned}F_{y\to x|z}^{(\tau)}&=\frac{1}{2\pi}\int_{-\pi}^{\pi}\ln\frac{G_{xx}^{(\tau)}(\omega)\Omega_{xx}^{(\tau)}G_{xx}^{(\tau)}(\omega)^{*}}{\bar{H}_{xx}^{(\tau)}(\omega)\Sigma_{xx}^{(\tau)}\bar{H}_{xx}^{(\tau)}(\omega)^{*}}\mathrm{d}\omega\\&=\frac{1}{2\pi}\int_{-\pi}^{\pi}\ln\frac{S_{xx}^{(\tau)}(\omega)}{\bar{H}_{xx}^{(\tau)}(\omega)\Sigma_{xx}^{(\tau)}\bar{H}_{xx}^{(\tau)}(\omega)^{*}}\mathrm{d}\omega\\&=F_{y\to x}^{(\tau)}.\end{aligned}$$

The second equality holds by applying the decomposition of $S_2^{(\tau)}(\omega)$ to get $S_{xx}^{(\tau)}(\omega)$.

Moreover, for multivariate variables $X_t=(x_t,y_t,z_{1t},z_{2t},\cdots,z_{nt})^{\top}$, Eq. (3.3) still holds. In this case, x_t and y_t are scalars while $z_t=(z_{1t},z_{2t},\cdots,z_{nt})^{\top}$ becomes a vector. And in the expression of $\hat{Q}_{xx}(f),\hat{\bar{H}}_{xx}(f)$ and $\hat{\bar{G}}_{xx}(f)$ are scalar while $\hat{\bar{G}}_{xz}(f)$ is a row vector, and $\hat{\bar{G}}_{zx}(f)$ and $\hat{\bar{H}}_{zx}(f)$ are column vectors, and $\hat{\bar{G}}_{zz}(f)$ is a matrix.

3.2 Asymptotic behavior of conditional GC verified using simulated data

In this section, we verify the asymptotic behavior of conditional GC by performing the GC analysis with different sampling intervals on the simulated data of the HH neural network model. We implemented the fourth order Runge-Kutta method with spike-spike correction technique [27] when simulating a 100-HH-neuron network driven by external Poisson inputs. The network consists of 80 excitatory and 20 inhibitory neurons randomly connected with 30% connection density. The parameters of the HH model used in simulation are listed in Table 1.

Table 1: The parameters of the HH model.

Parameters	**Meanings**	**Values**
F^{E}	strength of Poisson drive	$0.031\,\mathrm{mS}\cdot\mathrm{cm}^{-2}\cdot\mathrm{ms}^{-2}$
μ^{E}	rate of Poisson drive	$2.0\,\mathrm{kHz}$
S^{EE}	coupling strength from E to E neurons	$0.013\,\mathrm{mS}\cdot\mathrm{cm}^{-2}\cdot\mathrm{ms}^{-2}$
S^{IE}	coupling strength from E to I neurons	$0.013\,\mathrm{mS}\cdot\mathrm{cm}^{-2}\cdot\mathrm{ms}^{-2}$
S^{EI}	coupling strength from I to E neurons	$0.067\,\mathrm{mS}\cdot\mathrm{cm}^{-2}\cdot\mathrm{ms}^{-2}$
S^{II}	coupling strength from I to I neurons	$0.050\,\mathrm{mS}\cdot\mathrm{cm}^{-2}\cdot\mathrm{ms}^{-2}$
$\mathrm{d}t$	time step of numerical simulation	$0.025\,\mathrm{ms}$
τ	sampling interval	$0.1\,\mathrm{ms}$
T	length of time series	$4\times10^{5}\,\mathrm{ms}$

By simulating the HH network, as shown in Fig. 1(A), we observe the asynchronous state of the network, in which each neuron fires irregularly. The mean firing rates of neurons range from 24.78 Hz to 33.97 Hz, and their membrane potentials range from -11 mV to 105 mV with respect to the resting potential, which lies in the physiological regime of biological neurons. In addition, by changing the external input rate and connection strengths between neurons, the network will evolve into the synchronous state with neurons firing almost periodically, as shown in Fig. 1(B). In the following, we will verify the asymptotic behavior of conditional GC using the simulated data of both states, demonstrating that the asymptotic behavior we derived in Section 3.1 is generally valid.

Before performing the GC analysis, we first examine the stationarity of the time series as a prerequisite of the GC analysis. By dividing the time series of neural activity into five segments, and then computing and comparing the power spectrum of each segmental data, we observe the overlap of power spectrum densities across all segments, indicating the stationarity of the original time series. The results are shown in Fig. 6 in the Appendix A.

To perform the GC analysis, we shall determine the optimal regression order of joint regression. We estimate the optimal regression order for each different sampling interval τ using the Akaike information criterion (AIC), as shown in Fig. 7. We then investigate the asymptotic structure of the conditional GC value, i.e. the GC value is inversely proportional to the sampling interval τ. When the network is in the asynchronous state, by choosing different sampling intervals, we can obtain a set of conditional GC values as a function of the sampling interval. As shown in Fig. 2, the conditional GC value tends to zero linearly as the sampling interval τ approaches zero. Here we include four dif-

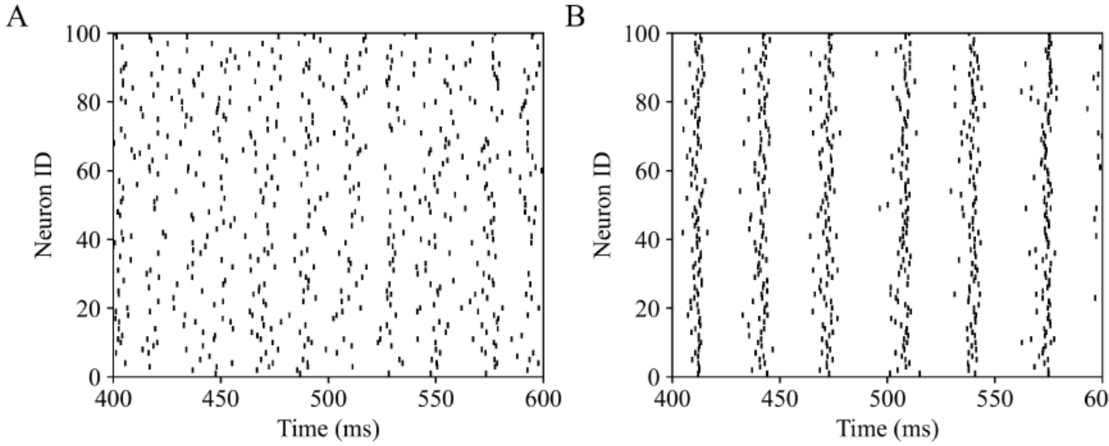

Figure 1: Rasters of the HH network in two dynamical regimes. Each dot corresponds to a Neuron's action potential. (A) Asynchronous state. The parameters for the asynchronous state are shown in Table 1. (B) Near-synchronous state. The parameters for the near-synchronous state are $F^{\mathrm{E}} = 0.02$ mS$\cdot$cm$^{-2}\cdot$ms^{-2}, $S^{\mathrm{EE}} = 0.06$ mS$\cdot$cm$^{-2}\cdot$ms^{-2}, $S^{\mathrm{IE}} = 0.05$ mS$\cdot$cm$^{-2}\cdot$ms^{-2}, $S^{\mathrm{EI}} = 0.06$ mS$\cdot$cm$^{-2}\cdot$ms^{-2}, and $S^{\mathrm{II}} = 0.07$ mS$\cdot$cm$^{-2}\cdot$ms^{-2}. Other parameters are the same as those in (A).

ferent pairs of neurons, covering all possible combinations of different types of neurons, and the conclusion above holds for all cases. To further verify the linear convergence, we plot the ratio between the conditional GC value over τ. As shown in the lower panel of Fig. 2, the flattened plateau in the GC curves for small τ again indicates the validity of the asymptotic behavior of the conditional GC value as $\tau \to 0$. Similar results have been observed in Fig. 3 when the network is in the near-synchronous state, demonstrating the asymptotic behavior is robust and general.

We further verify the validity of Eq. (3.3) derived in the previous section. By comparing the theoretical and numerical values of GC$/\tau$ (as $\tau \to 0$) based on the network simulations, as shown in Fig. 8 in Appendix B, the conditional GC value calculated numerically well consists with the theoretical one given by Eq. (3.3).

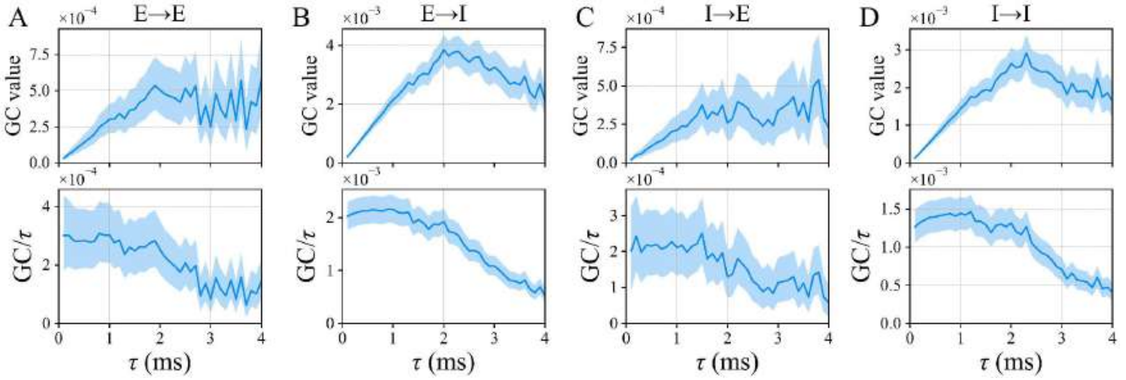

Figure 2: The dependence of the conditional GC value on sampling interval τ obtained from four pairs of neurons in the HH network in the asynchronous state. Upper panel: the relation between the conditional GC value and τ when analyzing the causal interaction from an E neuron to an E neuron, from an E neuron to an I neuron, from an I neuron to an E neuron, and from an I neuron to an I neuron. Lower panel: the ratio between the conditional GC value over τ is almost constant when τ approaches zero. The blue shadow represents the 95% confidence interval of the blue curve.

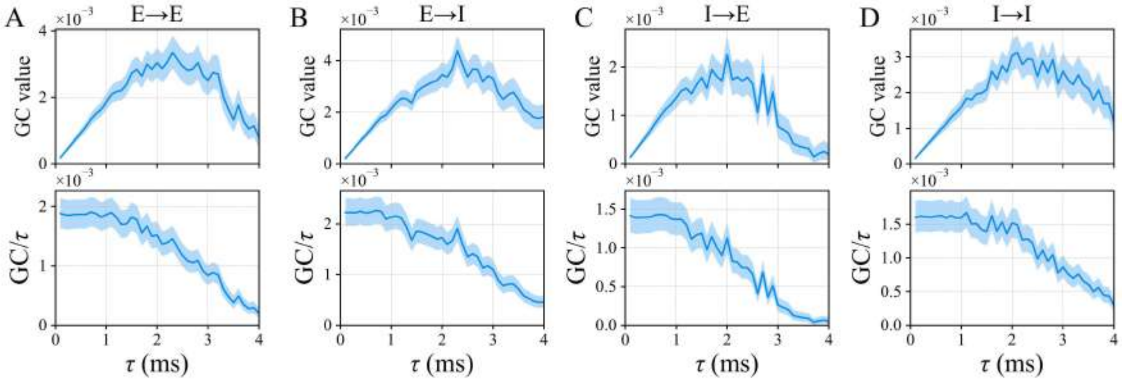

Figure 3: The dependence of the conditional GC value on sampling interval τ obtained from four pairs of neurons in the HH network in the near-synchronous state. Others are the same as in Fig. 2.

3.3 Asymptotic behavior of conditional GC verified using experimental data

In this section, we verify the asymptotic behavior of conditional GC by performing the GC analysis on the intracranial EEG (iEEG) data from Kaggle's contest project ("UPenn and Mayo Clinic's Seizure Detection Challenge") [3]. The iEEG data was measured from depth electrodes implanted along anterior-posterior axis of hippocampus and the subdural area of the brain during a seizure attack of epilepsy patients with temporal and extratemporal lob epilepsy. The data was recorded from 16 channels, with 5 kHz sampling frequency for each channel. The iEEG time series X_t, measured in the time period of 100-120 seconds after the onset of the seizure attack in a patient, will be used for the GC analysis below.

When analyzing the data, we first identify two artifacts in the raw data when plotting the power spectrum of all 16 channels. One artifact is the interference of alternating current (AC) in channel 2, as indicated by the periodic sharp peaks in the red curve shown in Fig. 4(A). We develop a protocol of nonlinear filtering to remove the frequency band contributed by AC (see details in the Appendix C). The blue curve in Fig. 4(A) is the resultant signal after removing the AC artifact. The other artifact is the abnormal discontinuity of the power spectrum at 1 kHz in channel 5, as shown in the red curve in Fig. 4(B). This discontinuity is typically caused by the quantization noise of the recorded signal, after a lowpass filtering at 1 kHz (see details in Appendix C and Fig. 9). To alleviate its contamination to the GC estimation, we use a 10-th order Butterworth lowpass filter at 530 Hz to avoid the aliasing effect as the blue curve shown in Fig. 4(B).

After removing the effect of artifacts from AC and quantization noise, we further denoise the data for the preparation of the GC analysis. We first downsample the data at 1 kHz, and then apply a de-noising operation to the down-sampled data using a linear reconstruction procedure as follows:

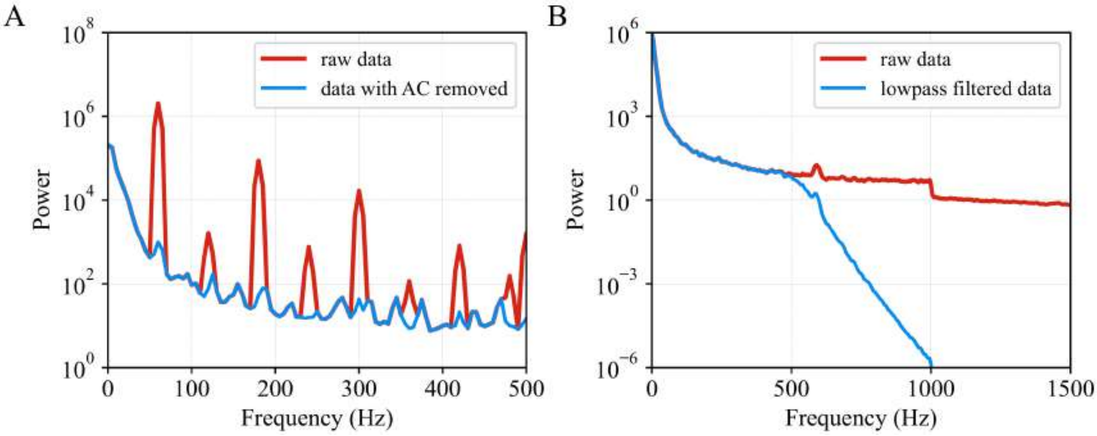

Figure 4: Power spectrum of raw data and processed data after removing artifacts. (A) Power spectrum of channel 2 before and after removing the AC signal. (B) Power spectrum of channel 5 before and after performing lowpass filtering.

1. Identify the optimal joint regression order m of the down-sampled data using the AIC.

2. Calculate the regression coefficient matrix of the joint regression $\hat{A}=(\hat{a}_{jk})$ and the covariance matrix $\hat{\Sigma}=(\hat{\sigma}_{pq})$ of residual.

3. (Permutation test) Shuffle the down-sampled data 1000 times, and calculate the regression coefficient for each shuffled data. Calculate the standard deviation s_{jk} and r_{pq} of $\hat{a}_{jk}$ and $\hat{\sigma}_{pq}$, respectively.

4. Truncate elements of $\hat{A}$ with absolute value smaller than $s_{jk}/10$ to zero, i.e. $\hat{a}^*_{jk}=\hat{a}_{jk}\mathbf{1}_{|a_{jk}|>=s_{jk}/10}$, and truncate elements of $\hat{\Sigma}$ with absolute value smaller than $r_{pq}/20$ to zero, i.e. $\hat{\sigma}^*_{pq}=\hat{\sigma}_{pq}\mathbf{1}_{|\sigma_{pq}|>=r_{pq}/20}$ (these non-significant coefficients are presumably caused by noise). Here, we denote the regression coefficient and covariance after truncation as $\hat{A}^*=(\hat{a}^*_{jk})$ and $\hat{\Sigma}^*=(\hat{\sigma}^*_{pq})$.

5. Generate new time series based on the same joint regression model using $\hat{A}^*$ and $\hat{\Sigma}^*$. Denote new time series as the reconstructed data.

By comparing the power spectrum and coherence (see Fig. 10 in Appendix D) of the down-sampled data and the reconstructed data, we find that the reconstructed data effectively captures the essential information in the down-sampled data, while with less noisy information.

After denoising, we also check the stationarity of the power spectrum of the reconstructed data as those done for the HH network case. The optimal regression order for each different sampling interval is estimated with the help of AIC, as shown in Fig. 7. The asymptotic behavior of the conditional GC value as the sampling interval approaches zero, obtained from analyzing the down-sampled data and the reconstructed data, is shown in Fig. 5.

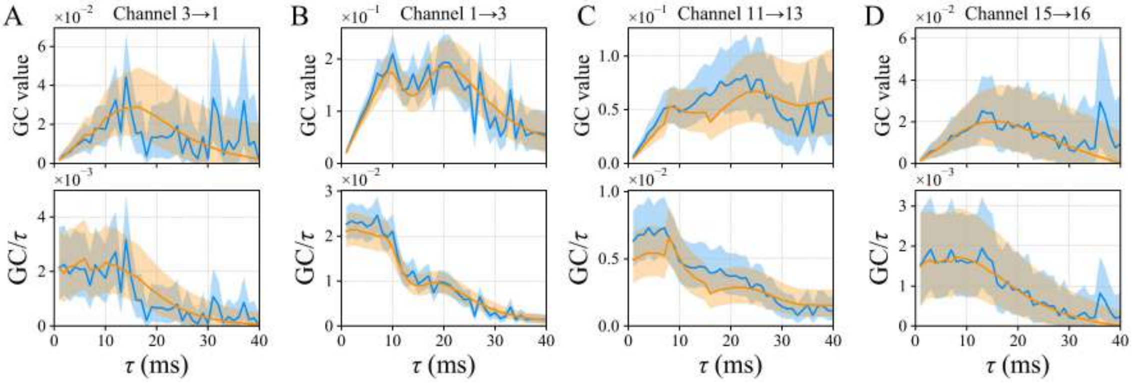

Figure 5: The dependence of the conditional GC value on sampling interval τ obtained from analyzing the experimental data. Upper panel: the relation between the conditional GC value and τ when analyzing the causal interaction from four pairs of channels. Lower panel: the ratio between the conditional GC value over τ is almost constant when τ approaches zero. Blue curves correspond to down-sampled data, and orange curves correspond to reconstructed data. The shadow represents the 95% confidence interval of the curve.

It is important to note that the conditional GC value from both the down-sampled data and the reconstructed data exhibit the characteristic of linear convergence, as depicted in Fig. 5 (upper panel). Moreover, when comparing with the down-sampled data (illustrated by the blue curves in Fig. 5), the reconstructed data (depicted by the orange curves in Fig. 5) displays a more prominent linear convergence structure. It suggests that the experimental data after denoising shows a clear inverse linear dependence on sampling interval when calculating the conditional GC value.

4 Discussion

Granger Causality has become a powerful statistical tool to analyze the directional causal interactions between nodes or signals in a system. However, there exists no general theoretical guarantee that GC can capture the causality for those complex systems as effectively as tools based on information theory [23], except for Gaussian random variables [1]. While previous works have shown that the GC analysis, albeit based on the linear regression model, is capable of inferring the causal connectivity in nonlinear systems such as neuronal networks, which can be further used to reconstruct the structural connectivity of networks [42]. In practice, the data analyzed by the GC method is measured with a finite sampling rate. Therefore, the GC value depends on the sampling interval. In a network with only two variables, it has been theoretically proved that the GC value decays linearly as the sampling interval approaches zero [45], and it has been verified on the simulated data of the integrate-and-fire neuronal networks [43]. Yet a theoretical foundation remains lacking whether this asymptotic behavior of the GC value exists for a system with more than two variables.

In this work, we have theoretically extended the asymptotic behavior of the GC value in the two-variable case to the general case of multiple variables. And we have numerically verified the asymptotic structure using simulated data from HH networks and using experimental data from the clinical iEEG signals. For the experimental data, with the help of nonlinear filtering and denoising through linear reconstruction protocol, we have alleviated the impact of artifacts and noise, and have identified a clear linear decay tendency of the conditional GC value as the sampling interval approaches zero.

Our analysis of how the conditional GC value depends on sampling interval is of great importance for the application of GC in real-world problems. For example, in neuroscience, unraveling the structural and functional connectivity of cortical networks has been under active investigations. Among many statistical methods, GC analysis is one of the most broadly used approaches to infer the structural and causal relation of large populations of neurons and brain areas. Intuitively, as the sampling rate becomes higher, the measured signal becomes more accurate to approximate the underlying continuous dynamics. However, our analysis and simulations have shown that the GC value will vanish in a linear fashion, indicating possible mis-inference of causality due to very small GC value even in the presence of causality. Based on the asymptotic structure of the conditional GC value, reliable estimations of causality can be achieved by calculating the ratio of GC over sampling interval for the sampling interval close to zero, a quantity independent of sampling interval.

Appendix A. Examination of the stationarity of time series

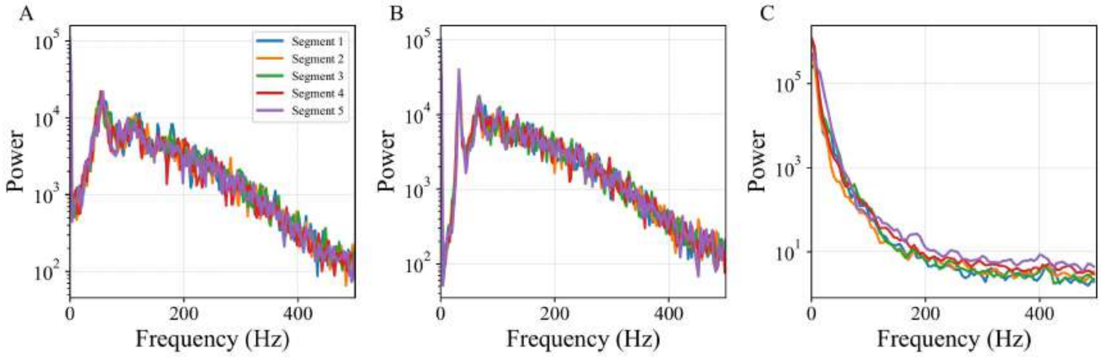

Figure 6: The power spectrums of sub-time-series for three dataset. A full-length time series is divided into five segments, and then the power spectrum of each segment is plotted. (A) Corresponds to the asynchronous HH network. (B) Corresponds to the near-synchronized HH network. (C) Corresponds to the iEEG signals measured in experiment.

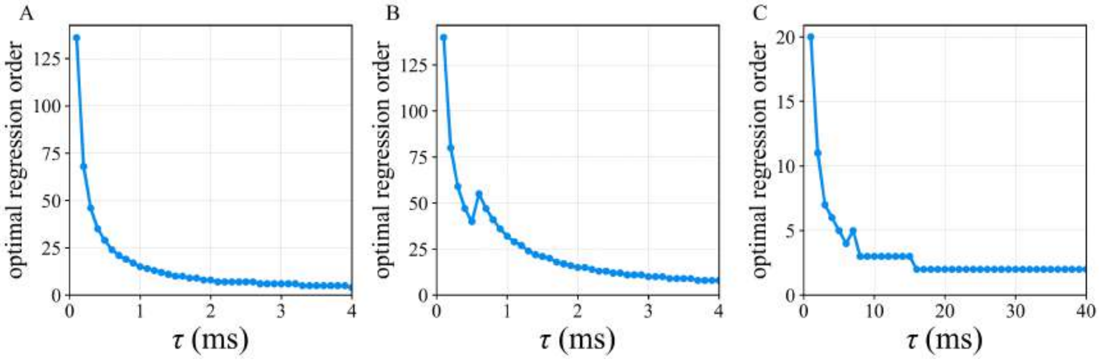

Figure 7: The optimal regression orders of "joint-regression" models (estimated by AIC) as functions of sampling intervals τ for three data sets. (A) Corresponds to the asynchronous HH network. (B) Corresponds to the synchronized HH network. (C) Corresponds to the iEEG signals measured in experiment.

Appendix B. Numerical verification of conditional GC expression

As a verification of Eq. 3.3, we compare the theoretical value and the numerical estimation of GC/τ (as $\tau \to 0$) in a smaller HH neuronal network, consisting of 7 excitatory neurons and 3 inhibitory neurons. As shown in Fig. 8, the theoretical value and the numerical calculation of GC/τ in the limit of $\tau \to 0$ almost overlap. This result also holds for larger networks since the derivation of Eq. 3.3 is independent of network size.

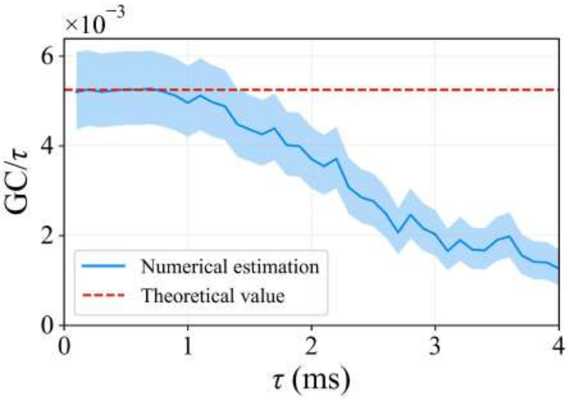

Figure 8: The theoretical value (red line) and the numerical calculation of GC/τ (blue curve) in the limit of $\tau \to 0$. The shadow represents the 95% confidence interval of the curve.

Appendix C. The artifacts in the iEEG data

Alternating current (AC) noise

In the raw iEEG data, some channels have strong AC interfere (some channels are not spoiled by AC at all). To remove the AC artifact, the basic idea is to estimate the component of the AC signal $g(t)$, and then subtract it, i.e.

$$x_{(\text{cleaned})}(t) = x(t) - g(t), \quad t = k\Delta t, \quad k \in \mathbb{N},$$

where $x(t)$ is the original signal, $x_{(\text{cleaned})}(t)$ is the processed signal after removing the AC noise. Here we model $g(t)$ in a general form as

$$g(t) = a(t)\cos\left(\phi(t) + w_0 t\right),$$

where w_0 is a constant, $a(t)$ and $\phi(t)$ are smooth functions. We use a cubic spline function with clamped boundary condition to model $a(t)$ and $\phi(t)$. $a(t)$ and $\phi(t)$ are assumed to be smooth as we have observed from the power spectrum of the iEEG data.

The central frequency w_0 is determined by finding the maximum of (Hanning) windowed Fourier transform

$$w_0 = \operatorname*{argmax}_{w} \left| \sum_{t=j\Delta t}^{T} x(t) q(t) e^{-\mathrm{i}wt} \right|^2,$$

DOI https://doi.org/10.4208/csiam-ls.SO-2024-0003

where

$$q(t) = \frac{1-\cos(2\pi t/T)}{2}.$$

With w_0 determined, the next step is to find $a(t)$ and $\phi(t)$ to minimize frequency components around w_0

$$\min_{a(t),\phi(t)} \sum_{k=k_L}^{k_N} \left| \sum_{t=j\Delta t}^{T} e^{-\mathrm{i}k\Delta wt} \big(x(t) - g(t)\big) \right|^2. \tag{C.1}$$

where $k_L = \lfloor (w_0 - w_{\text{width}}/2)/\Delta w \rfloor$, and $k_N = \lceil (w_0 + w_{\text{width}}/2)/\Delta w \rceil$. Here, Δw is the frequency step of discrete Fourier transform and w_{width} is the width of frequency band to be minimized, centered around w_0. Initial guess of $a(t)$ and $\phi(t)$ can be obtained by windowed Fourier transform at w_0: $ae^{\mathrm{i}\phi} = 2\sum_{t=j\Delta t}^{T} x(t) q(t) e^{-\mathrm{i}w_0 t}$.

In our numerical practice, we use one segmentation for the spline, i.e. cubic spline becomes a simple 3-rd order Hermite interpolation. Also note that there are peaks near the 50 Hz harmonics for signals from some channels, often only 0.2 Hz away. To further eliminate these artifacts, we perform the above procedure twice to the same harmonics.

Quantization noise

In the raw iEEG data, some channels show strong high-frequency power even after low-pass filtering. This ”strange” phenomenon is cased by quantization noise. In data processing, quantization noise refers to the error or distortion introduced when continuous or analog data is converted into a digital representation by quantization. This process involves truncating continuous data to discrete values with short significant digits.

To illustrate the artifact caused by quantization noise in our data, we design a toy model and generate a 20-second stationary time series X_t using a Gaussian regression model

$$X_t = A_1 X_{t-1} + A_2 X_{t-2} + \cdots + A_{19} X_{t-19} + \boldsymbol{\varepsilon}_t \tag{C.2}$$

with 1 kHz sampling frequency. We use the same regression coefficients and the same variance of the Gaussian white noise $\boldsymbol{\varepsilon}_t$ that fit the iEEG data introduced in the main text. We denote the generated data as D_1. The power spectrum of D_1 is shown as the blue curve in Fig. 9. Then, D_1 is filtered by a butterworth lowpass filter at $f < 250$ Hz to get a filtered data D_2. From the power spectrum (red curve in Fig. 9), we notice a sharp drop when the frequency passes 250 Hz due to the effect of low-pass filtering. Next, we truncate the significant digits of data points in D_2 to introduce the quantization noise and subsequently obtain data D_3. As shown in the orange curve in Fig. 9, the high frequency components ($f > 250$ Hz) of D_3 significantly increase, which is consistent with the feature in the power spectrum of channel 5 data in the iEEG dataset, which has been processed after low-pass filtering (see Fig. 4(B) red curve). Again to alleviate its contamination to the GC estimation, we apply a 10-th order Butterworth lowpass filter at 530 Hz on to the raw data as the blue curve shown in Fig. 4(B).

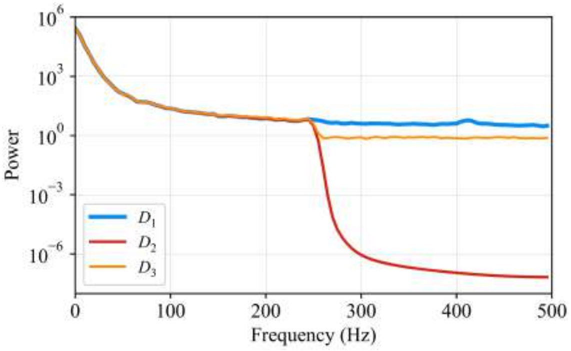

Figure 9: The influence of quantization noise on the power spectrum. $D1$ is the data generated by the regression model (Eq. (C.2)). $D2$ is the filtered data of $D1$ after a butterworth lowpass filter at $f<250\mathrm{Hz}$. $D3$ is obtained by truncating the significant digits of data points in D_2.

Appendix D. The spectrum analysis of the reconstructed data

As shown in Fig. 10, by comparing the power spectra between the down-sampled data and reconstructed data introduced in the main text, we show that the reconstructed data keeps the spectral information of down-sampled data. In addition, we define the coherence as the ratio between cross-spectrum and self power spectrum of time series

$$C(\omega)=\frac{S_{xy}(\omega)S_{yx}(\omega)}{S_{xx}(\omega)S_{yy}(\omega)},$$

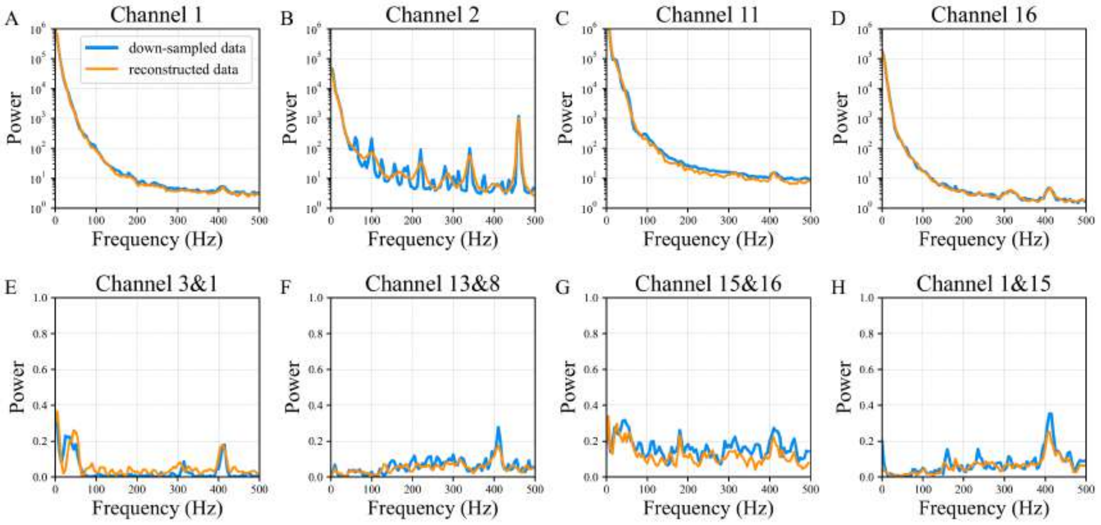

Figure 10: (A)-(D) Comparison of the power spectra between the down-sampled data and the reconstructed data from four representative channels of the iEEG data. (E)-(H) Comparison of the coherence curves of the down-sampled data and the reconstructed data from four pairs of representative channels of the iEEG data.

DOI https://doi.org/10.4208/csiam-ls.SO-2024-0003

which characterizes the correlation between time series across different frequencies. By comparing the coherence curves between the down-sampled data and reconstructed data, we show that the reconstructed data also keeps the correlation information of down-sampled data.

Acknowledgments

J. Mei and K. Chen contributed equally to the paper.

This work was supported by the Science and Technology Innovation 2030 – Brain Science and Brain-Inspired Intelligence Project (Grant No. 2021ZD0200204) and by the Lingang Laboratory (Grant No. LG-QS-202202-01) (S. Li, D. Zhou), by the National Natural Science Foundation of China (Grant Nos. 12271361, 12250710674) (S. Li), by the National Natural Science Foundation of China (Grant Nos. 12071287, 12225109) (D. Zhou), by the Shanghai Municipal Science and Technology Major Project 2021SHZDZX0102 and by the Student Innovation Center at Shanghai Jiao Tong University (J. Mei, K. Chen, S. Li, D. Zhou)

References

[1] L. Barnett, A. B. Barrett, and A. K. Seth, *Granger causality and transfer entropy are equivalent for Gaussian variables*, Phys. Rev. Lett., 103:238701, 2009.

[2] L. Barnett and A. K. Seth, *The MVGC multivariate Granger causality toolbox: A new approach to Granger-causal inference*, J. Neurosci. Methods, 223:50–68, 2014.

[3] bbrinkm, sbaldassano, and W. Cukierski, *UPenn and Mayo clinic's seizure detection challenge*, Kaggle, 2014. `https://kaggle.com/competitions/seizure-detection`

[4] I. Bojinov and N. Shephard, *Time series experiments and causal estimands: Exact randomization tests and trading*, J. Amer. Statist. Assoc., 114:1665–1682, 2019.

[5] S. L. Bressler and A. K. Seth, *Wiener-Granger causality: A well established methodology*, NeuroImage, 58:323–329, 2011.

[6] S. Cekic, D. Grandjean, and O. Renaud, *Multiscale Bayesian state-space model for Granger causality analysis of brain signal*, J. Appl. Stat., 46:66–84, 2019.

[7] F. Chen, J. Ke, R. Qi, Q. Xu, Y. Zhong, T. Liu, J. Li, L. Zhang, and G. Lu, *Increased inhibition of the amygdala by the mPFC may reflect a resilience factor in post-traumatic stress disorder: A resting-state fMRI Granger causality analysis*, Front. Psychiatry, 9:516, 2018.

[8] H. Cheng, D. Cai, and D. Zhou, *The extended Granger causality analysis for Hodgkin-Huxley neuronal models*, Chaos, 30:103102, 2020.

[9] D. Cohen and N. Tsuchiya, *The effect of common signals on power, coherence and Granger causality: Theoretical review, simulations, and empirical analysis of fruit fly LFPs data*, Front. Syst. Neurosci., 12:30, 2018.

[10] A. Compte, M. V. Sanchez-Vives, D. A. McCormick, and X. J. Wang, *Cellular and network mechanisms of slow oscillatory activity* $(<1\ Hz)$ *and wave propagations in a cortical network model*, J. Neurophysiol., 89:2707–2725, 2003.

[11] M. Dhamala, G. Rangarajan, and M. Ding, *Analyzing information flow in brain networks with nonparametric Granger causality*, NeuroImage, 41:354–362, 2008.

[12] M. Ding, Y. Chen, and S. L. Bressler, *Granger causality: Basic theory and application to neuroscience*, in: Handbook of Time Series Analysis: Recent Theoretical Developments and Applications, Wiley, 437–460, 2006.

[13] M. Ding and C. Wang, *Analyzing MEG data with Granger causality: Promises and pitfalls*, in: Magnetoencephalography, Springer, 647–657, 2019.

[14] K. J. Friston, *Functional and effective connectivity: A review*, Brain Connect., 1:13–36, 2011.

[15] W. Gerstner and W. M. Kistler, *Spiking Neuron Models: Single Neurons, Populations, Plasticity*, Cambridge University Press, 2002.

[16] J. F. Geweke, *Measures of conditional linear dependence and feedback between time series*, J. Amer. Statist. Assoc., 79:907–915, 1984.

[17] J. Guo, F. Fang, W. Wang, and F. Ren, *EEG emotion recognition based on Granger causality and CapsNet neural network*, in: 2018 5th IEEE International Conference on Cloud Computing and Intelligence Systems (CCIS), IEEE, 47–52, 2018.

[18] M. Hejazi and A. Motie Nasrabadi, *Prediction of epilepsy seizure from multi-channel electroencephalogram by effective connectivity analysis using Granger causality and directed transfer function methods*, Cogn. Neurodyn., 13:461–473, 2019.

[19] A. L. Hodgkin and A. F. Huxley, *The components of membrane conductance in the giant axon of Loligo*, J. Physiol., 116:473–496, 1952.

[20] A. L. Hodgkin and A. F. Huxley, *Propagation of electrical signals along giant nerve fibres*, Proc. R. Soc. Lond. B Biol. Sci., 140:177–183, 1952.

[21] A. L. Hodgkin and A. F. Huxley, *A quantitative description of membrane current and its application to conduction and excitation in nerve*, J. Physiol., 117:500–544, 1952.

[22] A. L. Hodgkin, A. F. Huxley, and B. Katz, *Measurement of current-voltage relations in the membrane of the giant axon of Loligo*, J. Physiol., 116:424–448, 1952.

[23] S. Li, Y. Xiao, D. Zhou, and D. Cai, *Causal inference in nonlinear systems: Granger causality versus time-delayed mutual information*, Phys. Rev. E, 97:052216, 2018.

[24] C. Luo, F. Li, P. Li, C. Yi, C. Li, Q. Tao, X. Zhang, Y. Si, D. Yao, G. Yin, P. Song, H. Wang, and P. Xu, *A survey of brain network analysis by electroencephalographic signals*, Cogn. Neurodyn., 16:17–41, 2022.

[25] P. Masani, *The prediction theory of multivariate stochastic processes, III*, Acta Math., 104:141–162, 1960.

[26] J. R. McCrorie and M. J. Chambers, *Granger causality and the sampling of economic processes*, J. Econometrics, 132:311–336, 2006.

[27] A. V. Rangan and D. Cai, *Fast numerical methods for simulating large-scale integrate-and-fire neuronal networks*, J. Comput. Neurosci., 22:81–100, 2007.

[28] P. Rangarajan and R. P. N. Rao, *Estimation of vector autoregressive parameters and Granger causality from noisy multichannel data*, IEEE Trans. Biomed. Eng., 66:2231–2240, 2019.

[29] H. P. Robinson and N. Kawai, *Injection of digitally synthesized synaptic conductance transients to measure the integrative properties of neurons*, J. Neurosci. Methods, 49:157–165, 1993.

[30] D. J. A. Smit, C. J. Stam, D. Posthuma, D. I. Boomsma, and E. J. C. De Geus, *Heritability of "small-world" networks in the brain: A graph theoretical analysis of resting-state EEG functional connectivity*, Hum. Brain Mapp., 29:1368–1378, 2008.

[31] V. Solo, *State-space analysis of Granger-Geweke causality measures with application to fMRI*, Neural Comput., 28:914–949, 2016.

[32] Y. Sun, D. Zhou, A. V. Rangan, and D. Cai, *Pseudo-Lyapunov exponents and predictability of Hodgkin-Huxley neuronal network dynamics*, J. Comput. Neurosci., 28:247–266, 2010.

[33] Z.-q. K. Tian, K. Chen, S. Li, D. W. McLaughlin, and D. Zhou, *Quantitative relations*

among causality measures with applications to pulse-output nonlinear network reconstruction, bioRxiv:2023.04.02.535284, 2023.
[34] P. P. Vaidyanathan, *The Theory of Linear Prediction*, in: Synthesis Lectures on Signal Processing, Springer, 2008.
[35] M. P. van den Heuvel and H. E. Hulshoff Pol, *Exploring the brain network: A review on resting-state fMRI functional connectivity*, Eur. Neuropsychopharmacol., 20:519–534, 2010.
[36] X. Wen, G. Rangarajan, and M. Ding, *Multivariate Granger causality: An estimation framework based on factorization of the spectral density matrix*, Philos. Trans. Roy. Soc. A, 371:20110610, 2013.
[37] X.-T. Wen, X.-J. Zhao, L. Yao, and X. Wu, *Applications of Granger causality model to connectivity network based on fMRI time series*, in: Advances in Natural Computation. ICNC 2006. Lecture Notes in Computer Science, Springer, 4221:205–213, 2006.
[38] N. Wiener and P. Masani, *The prediction theory of multivariate stochastic processes*, Acta Math., 98:111–150, 1957.
[39] N. Wiener and P. Masani, *The prediction theory of multivariate stochastic processes, II: The linear predictor*, Acta Math., 99:93–137, 1958.
[40] G. T. Wilson, *The factorization of matricial spectral densities*, SIAM J. Appl. Math., 23:420–426, 1972.
[41] C. Zhang, Q.-H. Lin, C.-Y. Zhang, Y.-G. Hao, X.-F. Gong, F. Cong, and V. D. Calhoun, *Comparison of functional network connectivity and Granger causality for resting state fMRI data*, in: Advances in Neural Networks – ISNN 2017, Springer, 559–566, 2017.
[42] D. Zhou, Y. Xiao, Y. Zhang, Z. Xu, and D. Cai, *Causal and structural connectivity of pulse-coupled nonlinear networks*, Phys. Rev. Lett., 111:54102, 2013.
[43] D. Zhou, Y. Xiao, Y. Zhang, Z. Xu, and D. Cai, *Granger causality network reconstruction of conductance-based integrate-and-fire neuronal systems*, PLoS ONE, 9(2):e87636, 2014.
[44] D. Zhou, Y. Zhang, Y. Xiao, and D. Cai, *Analysis of sampling artifacts on the Granger causality analysis for topology extraction of neuronal dynamics*, Front. Comput. Neurosci., 8:75, 2014.
[45] D. Zhou, Y. Zhang, Y. Xiao, and D. Cai, *Reliability of the Granger causality inference*, New J. Phys., 16:043016, 2014.

DOI https://doi.org/10.4208/csiam-ls.SO-2024-0003